Check for updates

optica

X-ray phase tomography with near-field speckles for three-dimensional virtual histology

Marie-Christine Zdora,[1,2,3,]* Pierre Thibault,[1,2] Willy Kuo,[4,5] Vincent Fernandez,[6]
Hans Deyhle,[2] Joan Vila-Comamala,[7] Margie P. Olbinado,[8,9] Alexander Rack,[9]
Peter M. Lackie,[10] Orestis L. Katsamenis,[11] Matthew J. Lawson,[10]
Vartan Kurtcuoglu,[4,5,12] Christoph Rau,[2] Franz Pfeiffer,[13,14] and Irene Zanette[1]

[1]School of Physics & Astronomy, University of Southampton, Highfield Campus, Southampton, SO17 1BJ, UK
[2]Diamond Light Source, Harwell Science and Innovation Campus, Didcot, OX11 0DE, UK
[3]Department of Physics & Astronomy, University College London, Gower Street, London, WC1E 6BT, UK
[4]The Interface Group, Institute of Physiology, University of Zurich, 8057 Zurich, Switzerland
[5]National Centre of Competence in Research, Kidney.CH, Zurich, Switzerland
[6]Imaging and Analysis Centre, Natural History Museum, London, SW7 5BD, UK
[7]Institute for Biomedical Engineering, ETH Zurich, 8092 Zurich, Switzerland
[8]Paul Scherrer Institute, 5232 Villigen PSI, Switzerland
[9]ESRF—The European Synchrotron, 38000 Grenoble, France
[10]Clinical and Experimental Sciences, Faculty of Medicine, University of Southampton, Southampton, SO17 1BJ, UK
[11]μ-VIS X-Ray Imaging Centre, Faculty of Engineering and Physical Sciences, University of Southampton, SO17 1BJ, UK
[12]Zurich Center for Integrative Human Physiology, University of Zurich, 8057 Zurich, Switzerland
[13]Chair of Biomedical Physics, Department of Physics and Munich School of BioEngineering, Technical University of Munich, 85748 Garching, Germany
[14]Department of Diagnostic and Interventional Radiology, Klinikum rechts der Isar, Technical University of Munich, 81675 Munich, Germany
*Corresponding author: m.zdora@soton.ac.uk

High-contrast, high-resolution imaging of biomedical specimens is indispensable for studying organ function and pathologies. Conventional histology, the gold standard for soft-tissue visualization, is limited by its anisotropic spatial resolution, elaborate sample preparation, and lack of quantitative image information. X-ray absorption or phase tomography have been identified as promising alternatives enabling non-destructive, distortion-free three-dimensional (3D) imaging. However, reaching sufficient contrast and resolution with a simple experimental procedure remains a major challenge. Here, we present a solution based on x-ray phase tomography through speckle-based imaging (SBI). We demonstrate on a mouse kidney that SBI delivers comprehensive 3D maps of hydrated, unstained soft tissue, revealing its microstructure and delivering quantitative tissue-density values at a density resolution of better than 2 mg/cm^3 and spatial resolution of better than 8 μm. We expect that SBI virtual histology will find widespread application in biomedicine and will open up new possibilities for research and histopathology.   © 2020 Optical Society of America under the terms of the OSA Open Access Publishing Agreement

https://doi.org/10.1364/OPTICA.399421

1. INTRODUCTION

The microscopic visualization of human and animal tissue is a fundamental part of pathological investigations in research and clinical practice. Studying alterations in tissue structure and composition can be key to identify the cause, stage, and progress of treatment of an illness. Revealing the internal organ structure requires imaging methods with high spatial resolution and high contrast for soft-tissue components, ideally capable of non-invasively providing undistorted three-dimensional (3D) information from hydrated specimens.

Conventional histological examination—using a light microscope to image stained thin slices of a specimen embedded in a hard matrix—has long been the biomedical standard and provides high-resolution images of the tissue. Particular components and cell types can be highlighted with different staining agents. However, typically only two-dimensional (2D) information can be extracted. Combining the 2D serial sections into a 3D volume is possible but time-consuming and often hindered by artefacts occurring during tissue preparation and sectioning [1]. Furthermore, the 3D volume generated from the sections does not provide isotropic spatial resolution, which is required for accurate and precise volumetric analysis.

A suitable method to extend and complement conventional histology is the use of x-ray micro computed tomography

(microCT) [2], which allows for non-destructive volumetric imaging at isotropic spatial resolution. While x-ray absorption-based microCT is widely applied in a variety of fields, the achievable image contrast is often too low for biomedical applications. Soft-tissue discrimination requires the use of contrast agents, and the visualization of blood vessels is commonly achieved by corrosion casting with a resin [3–9]. These approaches, however, bear the risk of altering the tissue structure, are susceptible to incomplete tissue or vessel penetration, and are often incompatible with complementary follow-up imaging techniques including conventional histology. Moreover, corrosion casting is only suitable for vessel imaging, as it dissolves the tissue and is therefore unable to visualize its structure.

Alternative x-ray methods based on extracting the x-ray phase shift induced by the sample [10] can provide significantly better contrast for soft biomedical tissue without the need for staining and have recently been identified as a promising approach for virtual histology [9,11–15]. However, the x-ray phase-contrast imaging methods employed for this purpose to date, such as propagation-based imaging (PBI) [16–18] and x-ray grating interferometry (XGI) [19–21], have various limitations that have prevented their practical use and wider uptake for virtual histology. These include an elaborate experimental setup with costly, absorbing x-ray optical elements and insufficient spatial resolution for XGI and constraints on the size and nature of the sample and non-quantitative results for PBI.

We here show that phase tomography based on x-ray speckle-based imaging (SBI) [22–24] has the potential to overcome these limitations and is a promising candidate for virtual histology applications. SBI is a recent x-ray phase-contrast imaging method based on a simple, cost-effective setup that does not require sophisticated optical elements or high-precision instrumentation. Merely a piece of sandpaper is added to the conventional x-ray imaging equipment. SBI, furthermore, does not impose strong restrictions on the properties of the x-ray beam [25–27] and the type of sample, making it widely accessible and applicable. Thanks to its high sensitivity, SBI is ideally suited for the investigation of specimens with small density differences.

The first demonstrations of SBI phase tomography were reported a few years ago [26,28]. However, its quantitative character, namely its ability to provide absolute, unbiased density information and enable the accurate measurement of 3D structures, has thus far not been explored. Moreover, while the potential of SBI for applications such as biomedical imaging has been identified in proof-of-principle demonstrations [28,29], sufficient image quality for a quantitative and scientifically relevant analysis has not been reported, to the best of our knowledge. Here, we demonstrate the unexplored potential of SBI x-ray phase tomography for the application of 3D virtual histology on a whole unstained, hydrated kidney of a healthy mouse imaged at a synchrotron radiation facility.

2. X-RAY SPECKLE-BASED PHASE TOMOGRAPHY

SBI is well suited for visualizing the structure of biomedical tissue on the micrometer scale, providing a phase sensitivity on the order of nanoradians in terms of x-ray refraction angle and a spatial resolution of a few micrometers at a field of view extending to several centimeters.
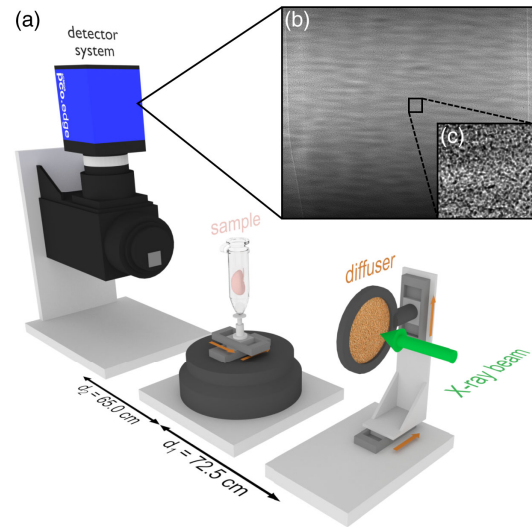
Fig. 1. Experimental setup for x-ray speckle-based phase tomography. (a) Setup for the measurement of the mouse kidney specimen. (b) One of the raw speckle projections acquired with the diffuser and the sample in the beam. (c) Zoomed region of the speckle pattern in panel (b).

The experimental setup for SBI phase tomography, see Fig. 1(a), is simple. The only addition to the standard x-ray tomography apparatus is a piece of abrasive paper used as a phase modulator, also called a diffuser. Scattering and subsequent interference of the x-rays from the small particles in the diffuser lead to the formation of a near-field speckle pattern [30], see Figs. 1(b) and 1(c), which acts as a wavefront marker. X-ray refraction in the sample results in a displacement of the speckle pattern with respect to its reference without a sample, which can be retrieved computationally and converted to a differential phase signal [22,23,31]. The speckle displacements s_x and s_y in the horizontal and vertical direction, respectively, obtained by the reconstruction algorithm are directly related to the x-ray refraction angles α_x, α_y under small-angle approximation and, subsequently, to the differential phase signals $\partial\Phi/\partial x$, $\partial\Phi/\partial y$:

$$\frac{\partial\Phi}{\partial x} = \frac{2\pi}{\lambda}\alpha_x = \frac{2\pi}{\lambda}\frac{s_x}{d_2},$$

$$\frac{\partial\Phi}{\partial y} = \frac{2\pi}{\lambda}\alpha_y = \frac{2\pi}{\lambda}\frac{s_y}{d_2}, \tag{1}$$

where λ is the x-ray wavelength, and d_2 is the sample detector distance. The differential phase images in the horizontal and vertical direction, as shown in Fig. S4 in Supplement 1, can be combined together via integration, here a Fourier integration routine [23,32]. The resulting phase shift signal Φ is directly related to the refractive index decrement δ, which is directly proportional to the electron density ρ_{el}, for energies far from the absorption edges [33]. Moreover, a linear relationship between ρ_{el} and the mass density ρ_m holds, see Supplement 1. A tomography scan consisting of 2D projections at different viewing angles of the sample delivers a 3D map of these quantities.

Among the various ways of performing SBI, we used our recently developed approach, the unified modulated pattern analysis (UMPA) [34]. It allows for multimodal signal retrieval by analyzing the sample-induced modulations of the speckle pattern using a least-squares minimization procedure. UMPA is a robust

yet flexible implementation that provides a trade-off between spatial resolution, phase sensitivity, and scan time [35] and does not rely on a motorized stage with nanometer precision required by some other SBI methods [31,36].

We carried out x-ray speckle-based phase tomography measurements at beamline ID19 of the European Synchrotron Radiation Facility (ESRF, Grenoble, France) using an x-ray beam with a narrow energy spectrum with a peak energy of 26.3 keV (see Supplement 1 for a detailed description of the parameters and data acquisition). The sample was mounted on a tomographic stage located $d_1 = 72.5$ cm downstream of the diffuser. Reference images (without the specimen in the beam) and sample images (with the specimen in the beam) were acquired at $N = 20$ different transverse positions of the diffuser. The resulting speckle interference patterns were recorded by a detection system placed $d_2 = 65.0$ cm downstream of the sample, with an effective pixel size of $p_{\text{eff}} = 3.1$ µm. The acquisition of the sample images was performed in tomographic mode by taking 2401 projections at equidistant viewing angles over 180 deg of sample rotation at each of the 20 diffuser positions.

3. RESULTS

A. Virtual Histology of the Murine Kidney

Using the UMPA implementation of SBI, we obtained the phase tomogram of a murine kidney. The virtual slices through the volume in Figs. 2(a) and 2(c)–2(e) contain detailed morphological information. The slice locations within the 3D volume are illustrated in Fig. S5 in Supplement 1. As the phase tomogram can be virtually sectioned along any desired plane, the correlation with slices obtained by conventional histology, which was performed on the same specimen after x-ray imaging (see Supplement 1), is

straightforward. The microstructural detail of the hydrated kidney tissue is clearly visualized in the phase volume slices and matches that seen by conventional histology with hemotoxylin and eosin (H&E) stain, see Figs. 2(b) and 2(f)–2(h). For better visualization and comparison, the phase volume images are presented in false colors similar to H&E-stained histology slices. While standard H&E staining for general microstructural overview was used in Fig. 2, histological slices with other common stains are shown in Fig. S6 in Supplement 1.

The four main regions of the kidney, characterized by the presence of different segments of the renal tubules, can be identified: inner medulla (IM), inner stripe of the outer medulla (ISOM), outer stripe of the outer medulla (OSOM), and cortex (COR). Essential microstructural features including small blood vessels, renal tubules, and renal glomeruli can be observed in the enlarged regions of interest (ROIs) in Figs. 2(e) and 2(h). The histological sections in Figs. 2(f)–2(h) show some tissue damage, folding, distortions, and overall shrinkage, here around 20%, which can be encountered in conventional histology due to the sample embedding and physical slicing processes [37].
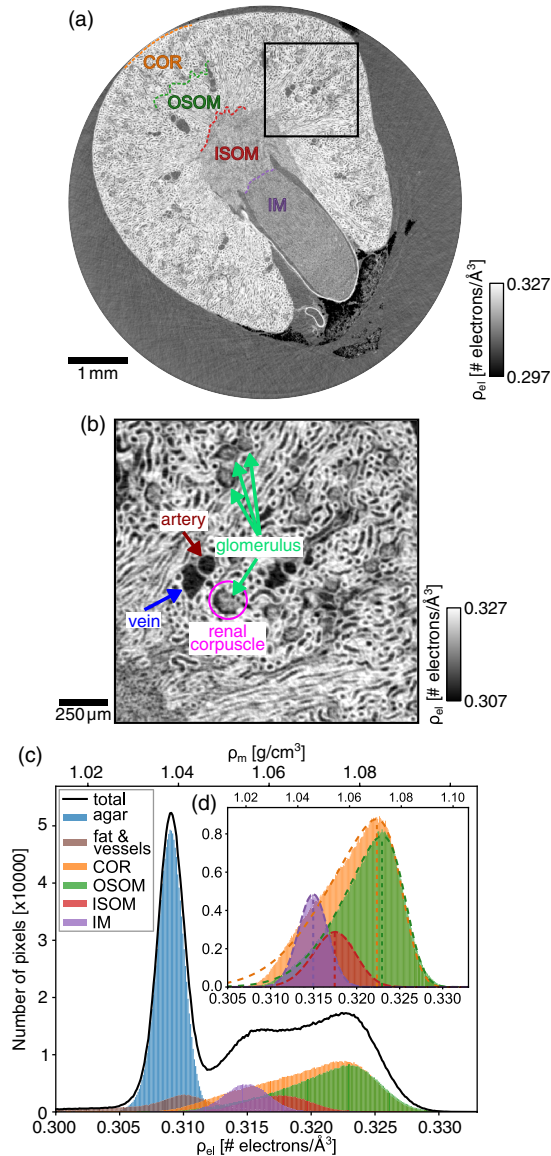
While conventional histology can achieve superior resolution in 2D, x-ray virtual histology based on SBI delivers the tissue structure in 3D and, in addition, provides absolute quantitative density information.

B. Quantitative Density Information from the Phase Volume

A section through the phase volume of the kidney after conversion to electron density values is shown in Fig. 3(a) and in more detail in Fig. 3(b). The high-density resolution allows for the discrimination of not only the fat, surrounding agar gel, and vessels in the sample, but also of the minute density differences between the four kidney
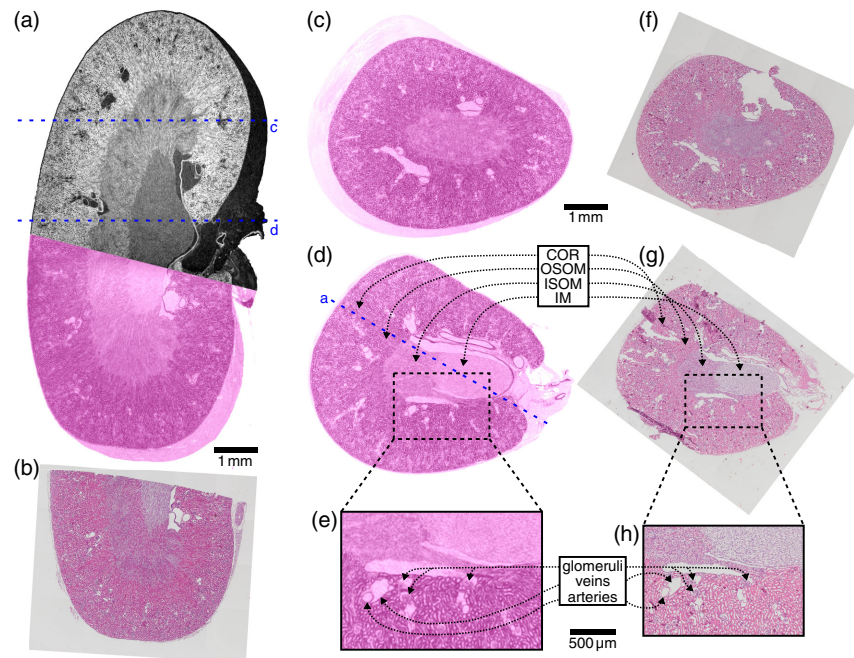
Fig. 2. Comparison of virtual phase volume slices and H&E-stained histological sections. (a) Long-axis cut through the phase volume (partly in false colors) and (b) corresponding histological slice (H&E staining, 10× magnification) of the same specimen. (c) and (d) Short-axis cuts through the phase volume [locations indicated in panel (a)] and (f) and (g) corresponding histological slices. The kidney regions, cortex (COR), outer stripe of the outer medulla (OSOM), inner stripe of the outer medulla (ISOM) and inner medulla (IM), can be identified. (e) and (h) Enlarged ROIs from panels (d) and (g) [panel (h) obtained with 20× magnification] visualizing fine details.

Table 1. Mass Density Values and Distribution Within the Different Kidney Regions[a, b, c, d]

Kidney Region	Density (g/cm³)	Range (mg/cm³)
IM	1.046	5.651 ± 0.011
ISOM	1.054	7.792 ± 0.028
OSOM	1.073	8.001 ± 0.020
COR	1.071	8.524 ± 0.043

[a]The density values were determined from the peak positions of the skewed Gaussian curves fitted to the histograms in Fig. 3(d).
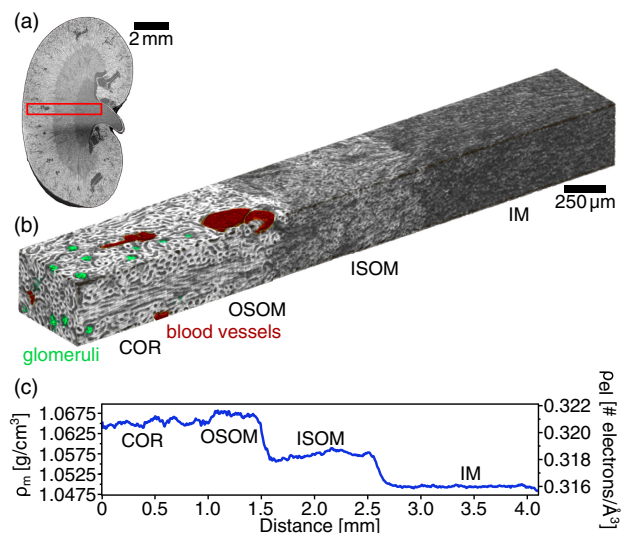
[b]The density-value ranges in the last column correspond to the one-standard-deviation ranges of normal Gaussian fit curves to the right slope of the histograms, see Fig. S3 in Supplement 1.

[c]Their uncertainties were determined from the co-variance matrices of the fit parameters via error propagation.

[d]The mass density differences between the kidney regions were found to be 8.3 mg/cm³ for IM-ISOM, 18.3mg/cm³ for ISOM-OSOM, and 2.0 mg/cm³ for OSOM-COR, which is consistent with the measurements by Shirai *et al*. reporting a density difference for OSOM-COR of 1.9 mg/cm³ for a hydrated formalin-fixed rat kidney [13].

tubule wall and lumen (see Supplement 1). The peak density values and the ranges of the distributions, which were determined from normal Gaussian fits to the right slope, are listed in Table 1.

In our experiment, we obtained a density resolution of better than 1.9 mg/cm³ for an estimated spatial resolution of approximately 8 μm (see Supplement 1). The latter is determined by the choice of reconstruction parameters in the UMPA analysis routine as well as the setup geometry and the resolution of the detector system. In particular, the spatial resolution in the 2D projections is typically limited by twice the full width at half-maximum (FWHM) of the analysis window in the UMPA reconstruction procedure [34]. While this does not match light microscopy capable of sub-cellular resolution, we can observe features down to the looped structure of the glomerular capillaries, see Fig. 3(b), the diameter of which can be estimated to be comparable to the

Fig. 3. Quantitative density analysis of the phase volume. (a) Slice through the electron density map of the kidney. The small density differences between the regions (COR, OSOM, ISOM, IM) can be resolved (black areas: peri-renal fat). (b) Enlarged ROI (COR/OSOM region) visualizing the network of the renal tubules, blood vessels, and glomeruli (renal corpuscle: glomerulus and surrounding Bowman's capsule). (c) Histograms of the electron and mass density distributions in the slice. (d) Histograms of the IM, ISOM, OSOM, and COR regions only. Skewed Gaussians were fitted to the histograms (dashed curves). Peak positions (vertical lines) and distribution widths can be found in Table 1.

regions. This is illustrated in the histograms of the whole slice [Fig. 3(c)] and of the kidney tissue only [Fig. 3(d)]. For the latter, pixels corresponding to fat, the surrounding agar gel, and vessels in the kidney were excluded via semi-automatic segmentation of the slice based on gray-value thresholding and manual refinement.

The peak positions [indicated by vertical dashed lines in Fig. 3(d)] were determined by fitting skewed Gaussians to the histograms of the kidney regions. The negative skewness of the distributions, most pronounced for the COR and OSOM, is caused by low-density contributions from the lumen (inner empty space) of the tubules as well as partial volume effects at the interface of the

Fig. 4. 3D quantitative density and structural information. (a) Location of a cuboid of interest in the phase volume. (b) 3D rendering of the cuboid. The arrangement of the tubules in the different kidney regions is visualized. Blood vessels (red) and glomeruli (green) can be identified and were segmented from the volume. (c) Line profile along the long axis of the cuboid, showing the mass and electron density values averaged over all slices along the short axes. Glomeruli and vessels were excluded for this analysis.
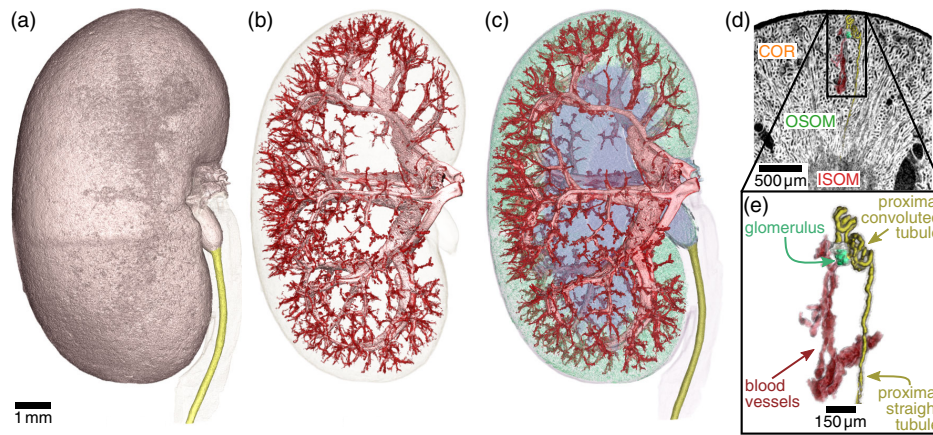
Fig. 5. 3D visualization and segmentation of the phase volume. (a) Renal capsule with ureter (yellow) and surrounding fatty tissue (semi-transparent gray). (b) Vascular network (arteries and veins) of the kidney extracted from the same data set. (c) Combined visualization of vascularization and tissue microstructure. A slice through the phase volume is shown in semi-transparent colors (blue, IM and ISOM; green, OSOM and COR). (d) Location of one renal nephron in the 3D phase volume and (e) segmented nephron consisting of blood vessel supply, glomerulus, and tubule (segmentation was terminated at the onset of the thin limb of the loop of Henle).

diameter of red blood cells [38], i.e., approximately 6–7 µm, just at the spatial resolution limit of our scan.

C. Three-Dimensional Analysis and Segmentation of Complex Networks

As illustrated for a volume of interest (VOI) of the tomogram in Fig. 4(b) and Visualization 1, the high contrast and 3D nature of the data allow for further analysis of the shape, size, and distribution of the functional elements within the organ such as the glomeruli and blood vessels. Retrieving this information reliably from 2D slices, as provided by conventional histology, can be extremely challenging.

As an example, we have measured the average glomerular diameter to be (97 ± 19) µm, based on 20 glomeruli. This is in agreement with the value (99 ± 13) µm (average over different regions) obtained in Ref. [39] by using light microscope images of osmium-stained kidney slices with subsequent alignment and computer-assisted tracing of tubules. Furthermore, as previously observed in the 2D tomogram slices in Fig. 3, the quantitative character of SBI allows for resolving and measuring the minute density differences between the kidney regions in the volume, see Fig. 4(c).

The 3D phase tomogram contains not only information about the internal features, but also the overall shape and volume of the specimen, see Fig. 5(a), which allows for the determination of its total volume, here 163.2 mm³. Obtaining this information on hydrated, unstained specimens gives an accurate and precise volume measure without the effects of tissue shrinkage, swelling, or distortions that can be encountered with other methods for tissue visualization that rely on dehydration or staining [7].

The interrelation and connectivity of essential elements of the organ, see Figs. 5(b)–5(e), which are not directly accessible by 2D conventional histology, can give valuable information on its function and health. Using semi-automatic segmentation based on intensity thresholding and region growing with commercially available software, we were able to visualize the blood vessel network of the kidney, see Fig. 5(b) and Visualization 2, simultaneously with the tissue microstructure, see Fig. 5(c) and Fig. S7 in

Supplement 1. It should be highlighted that in our measurements, unlike in other x-ray studies on visualizing the renal vascular network [40–43], neither contrast agent nor blood was present in the vessels, and the segmentation was solely possible because of the high image quality provided by SBI phase tomography.

The vessel network is directly connected to the renal tubules to enable filtration of the blood in the kidney. We were able to visualize the 3D structure of the tubular system down to a single renal nephron, the functional and structural unit of the kidney, as shown in Figs. 5(d) and 5(e). This is an important step towards studying the functional interrelation of the blood vessels, renal tubules, and collecting ducts in the kidney.

A summary of the 3D virtual histology results of the murine kidney is presented in Visualization 3.

4. DISCUSSION AND CONCLUSION

We have shown that x-ray speckle-based phase tomography is a strong contender for 3D virtual histology applications to complement, extend, and advance conventional histopathological investigations.

While biomedical research and clinical pathology currently make use solely of 2D tissue visualization as provided by conventional histology, the missing 3D information can be critical to obtain a full picture of the tissue morphology, organ volume, and sizes of structural elements in order to identify and quantify changes associated with pathologies. SBI phase tomography is able to provide this volumetric information on unstained, hydrated biomedical samples and has the potential to become a reliable tool for diagnostics and staging of diseases from excised tissue samples, in particular, as it is sensitive to changes in both tissue density and morphology. The absolute density values obtained by SBI provide an objective, quantitative physical measure for this purpose, enabling the unbiased, consistent, and reproducible evaluation of healthy and diseased animal and human tissue. These pathophysiological studies could then be validated and combined with subsequent analyses using complementary techniques including antibody-based and molecular biology-based histopathology.

Moreover, the ability of SBI phase tomography to visualize the tissue microstructure as well as the vascular network of an organ will allow for linking vasculature and organ function, which is an ongoing area of investigation, e.g., for the evaluation of the renal tubular function [44]. We have here performed the first step towards such studies by demonstrating the segmentation of the main renal blood vessel network and a single nephron up to the end of the proximal straight tubule. In the future, the extracted vessel and nephron networks could be the basis for advanced functional studies such as image-based fluid dynamics simulations to assess the overall kidney function and investigate poorly known mechanisms like renal oxygenation [45].

The non-destructive nature of SBI phase tomography makes it compatible with follow-up conventional histology investigations, which can be performed for validation purposes or additional functional information by using histochemical stains. A direct comparison of the virtual SBI phase tomogram slices and conventional histology slices could be performed in the future for a detailed study of tissue alterations induced by the dehydration, embedding, and slicing procedures required for the latter. As SBI can be applied to unstained or stained tissue embedded in hard, soft, or liquid matrices, it is expected to also be compatible with other follow-up imaging techniques, such as electron microscopy or optical tissue clearing.

SBI has the potential to overcome the main limitations of PBI and XGI for virtual histology. While PBI with a single-distance approach benefits from a simple setup, image reconstruction with the most commonly employed phase-retrieval algorithm [18] requires *a priori* information input based on the assumption of a homogeneous sample, rendering the method non-quantitative for complex specimens. Moreover, PBI is based on the Laplacian of the phase and is as such less sensitive to small density differences than differential phase methods like SBI and XGI, albeit providing a higher spatial resolution. XGI, on the other hand, does deliver quantitative phase information, but uses a more complicated, less robust setup that requires costly specialized absorbing x-ray optical elements, high-precision scanning stages and elaborate alignment procedures. The spatial and density resolution of both SBI and XGI depend on the experimental and setup conditions, the properties of the phase modulator (grating/diffuser), and for UMPA additionally on the reconstruction parameters [24,46,47]. In practice, the spatial resolution of SBI using UMPA is limited by the analysis window size, while for XGI the shear of the first-order diffracted beams created by the phase grating, which is dependent on the grating period, can become the limiting factor if it is larger than the resolution of the detector system. SBI combines the advantages of both XGI and PBI and provides high-sensitivity quantitative phase-contrast images with a simple setup that only requires a piece of sandpaper as an optical element.

The UMPA implementation of SBI has been particularly designed for robustness against potential setup instabilities, flexibility in the experimental arrangement, and data acquisition procedure, as well as the ability to fine-tune the spatial resolution and sensitivity of the phase-contrast images during the reconstruction process [34]. This makes UMPA swiftly adaptable to most existing x-ray imaging setups without additional specialized equipment.

We have here demonstrated the potential of SBI in the field of biomedicine as one of the most promising future applications of the technique. However, SBI is not limited to this area and can be applied to samples with a wide range of compositions and structures on the length scale of micrometers to centimeters. It is hence expected to find uptake in numerous other fields, such as palaeontology, earth sciences, engineering, and materials science.

Importantly, while the data presented here was acquired at a synchrotron source, SBI phase tomography is compatible with laboratory x-ray sources [25–27]. Although conventional laboratory sources will not enable the spatial and density resolution of synchrotron data, due to the reduced coherence properties, the shorter propagation distances, and increased blurring by the source, the quality of the results will be sufficiently high for many applications. Moreover, recently developed specialized x-ray sources with sub-micrometer spot sizes have shown to be a promising instrument for high-resolution x-ray virtual histology [48,49].

Once optimized at conventional x-ray systems, SBI phase tomography will become widely accessible and available for high-throughput applications in research, industry, and clinical pathology.

Disclosures. The authors declare no conflicts of interest.

See Supplement 1 for supporting content.

REFERENCES

1. J. Pichat, J. E. Iglesias, T. Yousry, S. Ourselin, and M. Modat, "A survey of methods for 3D histology reconstruction," Med. Image Anal. **46**, 73–105 (2018).
2. S. R. Stock, *MicroComputed Tomography: Methodology and Applications*, 2nd ed. (CRC Press, 2019).
3. B. D. Metscher, "MicroCT for developmental biology: a versatile tool for high-contrast 3D imaging at histological resolutions," Dev. Dyn. **238**, 632–640 (2009).
4. R. Wagner, D. Van Loo, F. Hossler, K. Czymmek, E. Pauwels, and L. Van Hoorebeke, "High-resolution imaging of kidney vascular corrosion casts with nano-CT," Microsc. Microanal. **17**, 215–219 (2011).
5. E. Pauwels, D. van Loo, P. Cornillie, L. Brabant, and L. van Hoorebeke, "An exploratory study of contrast agents for soft tissue visualization by means of high resolution x-ray computed tomography imaging," J. Microsc. **250**, 21–31 (2013).
6. J. M. de Souza e Silva, I. Zanette, P. B. Noël, M. B. Cardoso, M. A. Kimm, and F. Pfeiffer, "Three-dimensional non-destructive soft-tissue visualization with x-ray staining micro-tomography," Sci. Rep. **5**, 14088 (2015).
7. J. Missbach-Guentner, D. Pinkert-Leetsch, C. Dullin, R. Ufartes, D. Hornung, B. Tampe, M. Zeisberg, and F. Alves, "3D virtual histology of murine kidneys—high resolution visualization of pathological alterations by micro computed tomography," Sci. Rep. **8**, 1407 (2018).
8. M. Busse, M. Müller, M. A. Kimm, S. Ferstl, S. Allner, K. Achterhold, J. Herzen, and F. Pfeiffer, "Three-dimensional virtual histology enabled through cytoplasm-specific x-ray stain for microscopic and nanoscopic computed tomography," Proc. Natl. Acad. Sci. USA **115**, 2293–2298 (2018).
9. J. Albers, S. Pacilé, M. A. Markus, M. Wiart, G. Vande Velde, G. Tromba, and C. Dullin, "X-ray-based 3D virtual histology-adding the next dimension to histological analysis," Mol. Imaging Biol. **20**, 732–741 (2018).

10. S. W. Wilkins, Y. I. Nesterets, T. E. Gureyev, S. C. Mayo, A. Pogany, and A. W. Stevenson, "On the evolution and relative merits of hard x-ray phase-contrast imaging methods," Philos. Trans. R. Soc. A **372**, 20130021 (2014).

11. G. Schulz, T. Weitkamp, I. Zanette, F. Pfeiffer, F. Beckmann, C. David, S. Rutishauser, E. Reznikova, and B. Müller, "High-resolution tomographic imaging of a human cerebellum: comparison of absorption and grating-based phase contrast," J. R. Soc. Interface **7**, 1665–1676 (2010).

12. I. Zanette, T. Weitkamp, G. Le Duc, and F. Pfeiffer, "X-ray grating-based phase tomography for 3D histology," RSC Adv. **3**, 19816–19819 (2013).

13. R. Shirai, T. Kunii, A. Yoneyama, T. Ooizumi, H. Maruyama, T.-T. Lwin, K. Hyodo, and T. Takeda, "Enhanced renal image contrast by ethanol fixation in phase-contrast x-ray computed tomography," J. Synchrotron Radiat. **21**, 795–800 (2014).

14. M. Töpperwien, F. van der Meer, C. Stadelmann, and T. Salditt, "Three-dimensional virtual histology of human cerebellum by x-ray phase-contrast tomography," Proc. Natl. Acad. Sci. USA **115**, 6940–6945 (2018).

15. A. Khimchenko, C. Bikis, A. Pacureanu, S. E. Hieber, P. Thalmann, H. Deyhle, G. Schweighauser, J. Hench, S. Frank, M. Müller-Gerbl, G. Schulz, P. Cloetens, and B. Müller, "Hard x-ray nanoholotomography: large-scale, label-free, 3D neuroimaging beyond optical limit," Adv. Sci. **5**, 1700694 (2018).

16. A. Snigirev, I. Snigireva, V. Kohn, S. Kuznetsov, and I. Schelokov, "On the possibilities of x-ray phase contrast microimaging by coherent high-energy synchrotron radiation," Rev. Sci. Instrum. **66**, 5486–5492 (1995).

17. P. Cloetens, W. Ludwig, J. Baruchel, D. V. Dyck, J. V. Landuyt, J. P. Guigay, and M. Schlenker, "Holotomography: quantitative phase tomography with micrometer resolution using hard synchrotron radiation x rays," Appl. Phys. Lett. **75**, 2912–2914 (1999).

18. D. Paganin, S. C. Mayo, T. E. Gureyev, P. R. Miller, and S. W. Wilkins, "Simultaneous phase and amplitude extraction from a single defocused image of a homogeneous object," J. Microsc. **206**, 33–40 (2002).

19. A. Momose, "Phase-sensitive imaging and phase tomography using x-ray interferometers," Opt. Express **11**, 2303–2314 (2003).

20. T. Weitkamp, A. Diaz, C. David, F. Pfeiffer, M. Stampanoni, P. Cloetens, and E. Ziegler, "X-ray phase imaging with a grating interferometer," Opt. Express **13**, 6296–6304 (2005).

21. F. Pfeiffer, T. Weitkamp, O. Bunk, and C. David, "Phase retrieval and differential phase-contrast imaging with low-brilliance x-ray sources," Nat. Phys. **2**, 258–261 (2006).

22. S. Berujon, E. Ziegler, R. Cerbino, and L. Peverini, "Two-dimensional x-ray beam phase sensing," Phys. Rev. Lett. **108**, 158102 (2012).

23. K. S. Morgan, D. M. Paganin, and K. K. W. Siu, "X-ray phase imaging with a paper analyzer," Appl. Phys. Lett. **100**, 124102 (2012).

24. M.-C. Zdora, "State of the art of x-ray speckle-based phase-contrast and dark-field imaging," J. Imaging **4**, 60 (2018).

25. I. Zanette, T. Zhou, A. Burvall, U. Lundström, D. H. Larsson, M. Zdora, P. Thibault, F. Pfeiffer, and H. M. Hertz, "Speckle-based x-ray phase-contrast and dark-field imaging with a laboratory source," Phys. Rev. Lett. **112**, 253903 (2014).

26. I. Zanette, M.-C. Zdora, T. Zhou, A. Burvall, D. H. Larsson, P. Thibault, H. M. Hertz, and F. Pfeiffer, "X-ray microtomography using correlation of near-field speckles for material characterization," Proc. Natl. Acad. Sci. USA **112**, 12569–12573 (2015).

27. M.-C. Zdora, I. Zanette, T. Walker, N. W. Phillips, R. Smith, H. Deyhle, S. Ahmed, and P. Thibault, "X-ray phase imaging with the unified modulated pattern analysis of near-field speckles at a laboratory source," Appl. Opt. **59**, 2270–2275 (2020).

28. H. Wang, S. Berujon, J. Herzen, R. Atwood, D. Laundy, A. Hipp, and K. Sawhney, "X-ray phase contrast tomography by tracking near field speckle," Sci. Rep. **5**, 8762 (2015).

29. K. M. Pavlov, H. T. Li, D. M. Paganin, S. Berujon, H. Rougé-Labriet, and E. Brun, "Single-shot x-ray speckle-based imaging of a single-material object," Phys. Rev. Appl. **13**, 054023 (2020).

30. R. Cerbino, L. Peverini, M. A. C. Potenza, A. Robert, P. Bösecke, and M. Giglio, "X-ray-scattering information obtained from near-field speckle," Nat. Phys. **4**, 238–243 (2008).

31. S. Berujon, H. Wang, and K. Sawhney, "X-ray multimodal imaging using a random-phase object," Phys. Rev. A **86**, 063813 (2012).

32. C. Kottler, C. David, F. Pfeiffer, and O. Bunk, "A two-directional approach for grating based differential phase contrast imaging using hard x-rays," Opt. Express **15**, 1175–1181 (2007).

33. J. Als-Nielsen and D. McMorrow, *Elements of Modern X-ray Physics* (Wiley, 2011).

34. M.-C. Zdora, P. Thibault, T. Zhou, F. J. Koch, J. Romell, S. Sala, A. Last, C. Rau, and I. Zanette, "X-ray phase-contrast imaging and metrology through unified modulated pattern analysis," Phys. Rev. Lett. **118**, 203903 (2017).

35. M.-C. Zdora, P. Thibault, H. Deyhle, J. Vila-Comamala, C. Rau, and I. Zanette, "Tunable x-ray speckle-based phase-contrast and dark-field imaging using the unified modulated pattern analysis approach," J. Instrum. **13**, C05005 (2018).

36. H. Wang, Y. Kashyap, and K. Sawhney, "From synchrotron radiation to lab source: advanced speckle-based x-ray imaging using abrasive paper," Sci. Rep. **6**, 20476 (2016).

37. E. McInnes, "Artefacts in histopathology," Comp. Clin. Path. **13**, 100–108 (2005).

38. O. Smithies, "Why the kidney glomerulus does not clog: a gel permeation/diffusion hypothesis of renal function," Proc. Natl. Acad. Sci. USA **100**, 4108–4113 (2003).

39. X. Y. Zhai, H. Birn, K. B. Jensen, J. S. Thomsen, A. Andreasen, and E. I. Christensen, "Digital three-dimensional reconstruction and ultrastructure of the mouse proximal tubule," J. Am. Soc. Nephrol. **14**, 611–619 (2003).

40. M. D. Bentley, M. C. Ortiz, E. L. Ritman, and J. C. Romero, "The use of microcomputed tomography to study microvasculature in small rodents," Am. J. Physiol. Regul. Integr. Comp. Physiol. **282**, R1267–R1279 (2002).

41. L. Zagorchev, P. Oses, Z. W. Zhuang, K. Moodie, M. J. Mulligan-Kehoe, M. Simons, and T. Couffinhal, "Micro computed tomography for vascular exploration," J. Angiogenes. Res. **2**, 7 (2010).

42. U. Lundström, D. H. Larsson, A. Burvall, P. A. C. Takman, L. Scott, H. Brismar, and H. M. Hertz, "X-ray phase contrast for CO_2 microangiography," Phys. Med. Biol. **57**, 2603 (2012).

43. R. Hlushchuk, D. Haberthür, and V. Djonov, "Ex vivo microangioCT: advances in microvascular imaging," Vasc. Pharmacol. **112**, 2–7 (2019).

44. D. A. Ferenbach and J. V. Bonventre, "Kidney tubules: intertubular, vascular, and glomerular cross-talk," Curr. Opin. Nephrol. Hypertens. **25**, 194–202 (2016).

45. A. T. Layton, "Modeling transport and flow regulatory mechanisms of the kidney," ISRN Biomath. **2012**, 170594 (2012).

46. Y. Kashyap, H. Wang, and K. Sawhney, "Experimental comparison between speckle and grating-based imaging technique using synchrotron radiation x-rays," Opt. Express **24**, 18664–18673 (2016).

47. P. Modregger, B. R. Pinzer, T. Thüring, S. Rutishauser, C. David, and M. Stampanoni, "Sensitivity of x-ray grating interferometry," Opt. Express **19**, 18324–18338 (2011).

48. M. Reichardt, M. Töpperwien, A. Khan, F. Alves, and T. Salditt, "Fiber orientation in a whole mouse heart reconstructed by laboratory phase-contrast micro-CT," J. Med. Imaging **7**, 1–16 (2020).

49. M. Eckermann, M. Töpperwien, A.-L. Robisch, F. van der Meer, C. Stadelmann, and T. Salditt, "Phase-contrast x-ray tomography of neuronal tissue at laboratory sources with submicron resolution," J. Med. Imaging **7**, 1–15 (2020).